Modal analysis of enhanced absorption in silicon nanowire arrays

Björn C. P. Sturmberg,[1,*] **Kokou B. Dossou,**[2] **Lindsay C. Botten,**[2]
Ara A. Asatryan,[2] **Christopher G. Poulton,**[2] **C. Martijn de Sterke,**[1]
and Ross C. McPhedran[1]

[1]*CUDOS and IPOS, School of Physics, University of Sydney, 2006, Australia*
[2]*CUDOS, School of Mathematical Sciences, UTS, Sydney, 2007, Australia*
*b.sturmberg@physics.usyd.edu.au

Abstract: We analyze the absorption of solar radiation by silicon nanowire arrays, which are being considered for photovoltaic applications. These structures have been shown to have enhanced absorption compared with thin films, however the mechanism responsible for this is not understood. Using a new, semi-analytic model, we show that the enhanced absorption can be attributed to a few modes of the array, which couple well to incident light, overlap well with the nanowires, and exhibit strong Fabry-Pérot resonances. For some wavelengths the absorption is further enhanced by slow light effects. We study the evolution of these modes with wavelength to explain the various features of the absorption spectra, focusing first on a dilute array at normal incidence, before generalizing to a dense array and off-normal angles of incidence. The understanding developed will allow for optimization of simple SiNW arrays, as well as the development of more advanced designs.

References and links

1. N. S. Lewis, "Toward cost-effective solar energy use," Science **315**, 798–801 (2007).
2. L. Tsakalakos, "Nanostructures for photovoltaics," Mater. Sci. Eng. R **62**, 175–189 (2008).
3. O. Gunawan, K. Wang, B. Fallahazad, Y. Zhang, E. Tutuc, and S. Guha, "High performance wire-array silicon solar cells," Prog. Photovolt. Res. Appl. **10**, 1002 (2010).
4. K. R. Catchpole and A. Polman, "Plasmonic solar cells," Opt. Express **16**, 21793–217800 (2008).
5. H. A. Atwater and A. Polman, "Plasmonics for improved photovoltaic devices." Nat. Mater. **9**, 205–213 (2010).
6. L. Zeng, Y. Yi, C. Hong, J. Liu, N. Feng, X. Duan, and L. C. Kimerling, "Efficiency enhancement in Si solar cells by textured photonic crystal back reflector," Appl. Phys. Lett. **89**, 111111 (2006).
7. P. Bermel, C. Luo, L. Zeng, L. C. Kimerling, and J. D. Joannopoulos, "Improving thin-film crystalline silicon solar cell efficiencies with photonic crystals," Opt. Express **15**, 16986 (2007).
8. R. A. Pala, J. S. White, E. Barnard, J. Liu, and M. L. Brongersma, "Design of plasmonic thin-film Solar cells with broadband absorption enhancements," Adv. Mater. **21**, 3504–3509 (2009).
9. Z. Yu, A. Raman, and S. Fan, "Fundamental limit of light trapping in grating structures," Opt. Express **18**, 366–380 (2010).
10. E. Yablonovitch and G. D. Cody, "Intensity enhancement in textured optical sheets for solar cells," IEEE Trans. Electron. Dev. **29**, 300–305 (1982).
11. K. Peng, Y. Xu, Y. Wu, and Y. Yan, "Aligned single-crystalline Si nanowire arrays for photovoltaic applications," Small **1**, 1062–1067 (2005).
12. C. Lin and M. L. Povinelli, "Optical absorption enhancement in silicon nanowire arrays with a large lattice constant for photovoltaic applications," Opt. Express **17**, 19371–19381 (2009).

13. Z. Fan, H. Razavi, J. Do, A. Moriwaki, O. Ergen, Y.-L. Chueh, P. W. Leu, J. C. Ho, T. Takahashi, L. A. Reichertz, S. Neale, K. Yu, M. Wu, J. W. Ager, and A. Javey, "Three-dimensional nanopillar-array photovoltaics on low-cost and flexible substrates," Nat. Mater. **8**, 648–53 (2009).
14. E. C. Garnett and P. Yang, "Light trapping in silicon nanowire solar cells," Nano Lett. **10**, 1082–1087 (2010).
15. B. M. Kayes, M. A. Filler, M. C. Putnam, M. D. Kelzenberg, N. S. Lewis, and H. A. Atwater, "Growth of vertically aligned Si wire arrays over large areas (> 1 cm^2) with Au and Cu catalysts," Appl. Phys. Lett. **91**, 103110 (2007).
16. M. D. Kelzenberg, S. W. Boettcher, J. A. Petykiewicz, D. B. Turner-Evans, M. C. Putnam, E. L. Warren, J. M. Spurgeon, R. M. Briggs, N. S. Lewis, and H. A. Atwater, "Enhanced absorption and carrier collection in Si wire arrays for photovoltaic applications," Nat. Mater. **9**, 239–244 (2010).
17. B. M. Kayes, H. A. Atwater, and N. S. Lewis, "Comparison of the device physics principles of planar and radial p-n junction nanorod solar cells," J. Appl. Phys. **97**, 114302 (2005).
18. E. C. Garnett and P. Yang, "Silicon nanowire radial p-n junction solar cells." J. Am. Chem. Soc. **130**, 9224–9225 (2008).
19. Q. G. Du, C. H. Kam, H. V. Demir, H. Y. Yu, and X. W. Sun, "Broadband absorption enhancement in randomly positioned silicon nanowire arrays for solar cell applications," Opt. Lett. **36**, 1884–1886 (2011).
20. P. P. Altermatt, Y. Yang, T. Langer, A. Schenk, and R. Brendel, "Simulation of optical properties of Si wire cells," Conf. Proc. 34th IEEE PVSC, 972–977 (2009).
21. J. Li, H. Yu, M. Wong, X. Li, and G. Zhang, "Design guidelines of periodic Si nanowire arrays for solar cell application," Appl. Phys. Lett. **95**, 243113 (2009).
22. L. Hu and G. Chen, "Analysis of optical absorption in silicon nanowire arrays for photovoltaic applications," Nano Lett. **7**, 3249–3252 (2007).
23. E. Yablonovitch, "Statistical ray optics," J. Opt. Soc. Am. **72**, 899–907 (1982).
24. E. D. Kosten, E. L. Warren, and H. A. Atwater, "Ray optical light trapping in silicon microwires: exceeding the 2n^2 intensity limit," Opt. Express **19**, 3316–3331 (2011).
25. J. Kupec and B. Witzigmann, "Dispersion, wave propagation and efficiency analysis of nanowire solar cells," Opt. Express **17**, 10399–10410 (2009).
26. K. R. Catchpole, S. Mokkapati, and F. J. Beck, "Comparing nanowire, multi-junction and single junction solar cells in the presence of light trapping," J. Appl. Phys. **109**, 084519 (2011).
27. K. Dossou, L. C. Botten, A. A. Asatryan, B. P. C. Sturmberg, M. A. Byrne, C. G. Poulton, R. C. McPhedran, and C. M. de Sterke, "Modal formulation for scattering by absorbing photonic crystal slabs," in preparation.
28. M. A. Green and M. J. Keevers, "Optical properties of intrinsic silicon at 300 K," Prog. Photovolt. Res. Appl. **3**, 189–192 (1995).
29. K. B. Dossou and M. Fontaine, "A high order isoparametric finite element method for the computation of waveguide modes," Comput. Method Appl. M. **194**, 837–858 (2005).
30. L. C. Botten, T. P. White, A. A. Asatryan, T. Langtry, C. M. de Sterke, and R. C. McPhedran, "Bloch mode scattering matrix methods for modeling extended photonic crystal structures. I. Theory," Phys. Rev. E **70**, 1–13 (2004).
31. L. C. Botten, M. S. Craig, R. C. McPhedran, J. L. Adams, and J. R. Andrewartha, "The finitely conducting lamellar diffraction grating," Opt. Acta **28**, 1087–1102 (1981).
32. W. Shockley and H. J. Queisser, "Detailed balance limit of efficiency of p-n junction solar cells," J. Appl. Phys. **32**, 510–519 (1961).
33. ASTM, "Reference Solar Spectral Irradiance: Air Mass 1.5 Spectra," http://rredc.nreal.gov/solar/spectra/am1.5 .
34. G. H. Derrick and R. C. McPhedran, "Coated crossed gratings," J. Opt. **15**, 69–81 (1984).
35. K. Seo, M. Wober, P. Steinvurzel, E. Schonbrun, Y. Dan, T. Ellenbogen, and K. B. Crozier, "Multicolored Vertical Silicon Nanowires." Nano Lett. **11**, 1851–1856 (2011).
36. T. Baba, "Slow light in photonic crystals," Nat. Photonics **2**, 465–473 (2008).
37. A. Movchan, N. Movchan, and C. Poulton, *Asymptotic Models of Fields in Dilute and Densely Packed Composites* (Imperial College Press, 2002), Chap. 3.
38. R. C. McPhedran, N. A. Nicorovici, L. C. Botten, and K. A. Grubits, "Lattice sums for gratings and arrays," J. Math. Phys. **41**, 7808-16 (2000).
39. S. E. Han and G. Chen, "Optical absorption enhancement in silicon nanohole arrays for solar photovoltaics," Nano Lett. **10**, 1012–1015 (2010).
40. R. C. McPhedran and W. T. Perrins, "Electrostatic and optical resonances of cylinder pairs," Appl. Phys. **24**, 311–318 (1981).

1. Introduction

Nanostructured photovoltaics promise to simultaneously increase the efficiency and decrease the cost of solar cells [1, 2]. The incorporation of nanostructures in silicon photovoltaics is of particular importance as these currently make up over 80% of the photovoltaic market [3] due

to silicon's low cost, natural abundance, nontoxicity, and compatibility with mature fabrication techniques. Silicon, however absorbs poorly over the peak of the solar spectrum, requiring the use of over 100 μm thick Si wafers for sufficient absorption. This large thickness necessitates that the silicon be of a high chemical purity, for efficient carrier diffusion across the wafer [2], and such thick, high quality wafers currently account for almost half the cost of solar modules [3].

The incorporation of nanostructures allows the thickness of the absorbing layer to be reduced to a few micrometers, whilst remaining optically thick due to strong light trapping, leading to markedly reduced costs. Examples of such nanostructures include plasmonic light scattering particles [4, 5] and photonic crystal back or front surfaces [6, 7]. Light trapping in these structures has been shown to produce absorption enhancements of over 45% [8] and 31% [7] respectively. The full potential of nanostructured photovoltaics is illustrated by the absorption enhancement limit derived by Yu *et al*. for nanostructures in the wave-optics regime [9], which is significantly higher than the ray-optics-based Yablonovitch limit of $4n^2$, where n is the refractive index of the material [10].

A more recently developed nanostructure, the absorption enhancement of which has the potential to exceed that of plasmonics and photonic crystal reflectors, consists of a vertically aligned silicon nanowire (SiNW) array [11, 12]. This structure has been fabricated on silicon, glass and metal substrates using etching [11, 13, 14] as well as growth [15, 16] techniques that are scalable to large areas. Fabricated samples show strong light trapping, with path length enhancement factors of up to 73 [14]. In addition to their advantageous optical properties, SiNW arrays can decouple the directions of photon absorption and charge transport by the incorporation of radial p-n junctions [17, 18]. Using such junctions, SiNW array solar cells have been realized that outperform equally thick planar cells in measured power conversion efficiency [3].

An outstanding problem, the resolution of which is critical for the further development of SiNW array photovoltaics, is the physical understanding of the absorption enhancement mechanism of these arrays. This is a complex task due to the interplay of a multitude of effects, which include the propagation of energy along the nanowires, diffraction by the periodic array, and Fabry-Pérot-type resonances caused by reflections off the top and bottom interfaces, all of which are strongly wavelength dependent. To date numerical investigations have used the finite-difference time-domain method (FDTD) [19], the finite element method (FEM) [20, 21] and the transfer matrix method [12, 22] to calculate the reflectance, transmittance and absorptance of arrays, along with the total field distributions, whilst dispersive band structures have been calculated using FDTD [12]. These are all purely numerical approaches which can require substantial computational resources, and importantly, the results of which cannot isolate the various photonic effects, allowing for only general statements about suppressed reflection, optical concentration and the excitation of guided resonance modes [12, 16, 21].

Our general approach is to solve the Maxwell equations for the electric field, with the appropriate constitutive relation describing the optical properties of silicon, and then to extract the absorption from these results. This contrasts a statistical approach pioneered by Yablonovitch [23], and applied to SiNW arrays by Kosten *et al*. [24]. In their approach the reflection of light at interfaces is assumed to be Lambertian, so that the direction of the light inside the structure is random, whereas its further propagation follows from geometrical optics. Such an approach is therefore best-suited for large inclusions where interference and diffraction effects are least important.

Here we present a comprehensive description of the optical properties of SiNW arrays using a semi-analytic modal method, where the fields in the array are written as a superposition of Bloch modes. The modal nature of light propagation through nanowire arrays was studied previously at normal incidence for InP rather than for silicon [25], though the detailed absorption
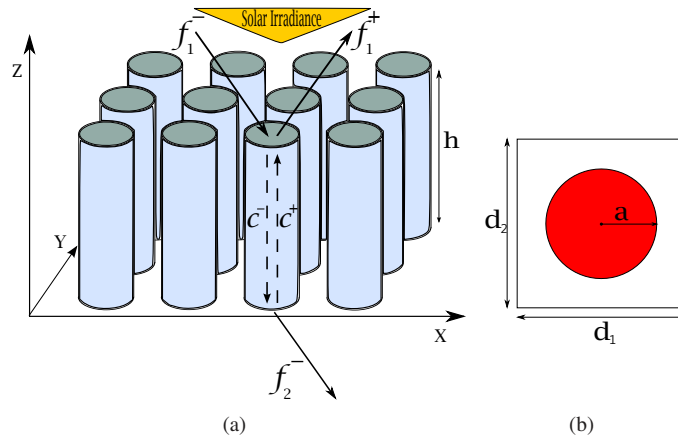
Fig. 1. (a) Schematic of SiNW array showing direction of irradiation and nanowire length, h. We indicate the fields by f for plane waves and c for Bloch modes, where $\pm$ indicates direction of propagation. (b) Unit cell reduction of SiNW array with radius a and lattice constants $d_{1,2}$ marked. For the square array $d_1 = d_2 = d$.

enhancement mechanism was not further explored, and the method employed does not apply to wavelengths where the intrinsic material absorption is low. For this reason, the Fabry-Pérot-like enhancement which we report and discuss in Sects. 3 and 4 could not be observed. By calculating the properties of the individual Bloch modes, including their propagation, reflections and their fields, we clarify the role of the physical effects and the importance of specific modes to the SiNW array absorption. We show that the absorption process is dominated by a few select modes, and that these modes absorb well due to good coupling to the incident field, high concentration within the nanowires, and strong Fabry-Pérot resonances. We concentrate on optical effects and exclude any consideration of the electrical performance of the arrays (for discussions of which see Refs. [17, 26]).

After outlining the simulation method in Sect. 2, we illustrate the properties and importance of specific modes in Sect. 3. We do this initially by the study of a dilute array, the absorption spectrum of which shows clear features, including a pronounced absorption peak at wavelengths above 595 nm, where bulk silicon absorbs poorly. In Sect. 4, the understanding gained from the dilute array is applied to a dense array of larger radii nanowires, with increased solar energy conversion efficiency. The analyses of Sects. 3 and 4 are for normally incident light only, and in Sect. 5 we consider non-normal incidence, before concluding in Sect. 6.

2. Modal Method

In order to carry out a modal analysis of SiNW arrays we develop a numerical method that combines the semi-analytic modal method with a vectorial FEM calculation. This method is briefly outlined below, leaving the details of the formulation and numerical implementation for a future publication [27]. Unlike previous studies [12, 22], we use the FEM only to calculate the Bloch modes. In contrast, the total fields and all other quantities, including the mode amplitude and their absorption, follow from the modal method. This requires calculating scattering matrices from the overlap of the Bloch modes with plane wave fields. Using this approach the calculation time is independent of the length of the array.

To focus on the essential physics of the SiNW array, following Refs. [12, 22], we model the silicon nanowires as surrounded by an air background and the array as suspended in air, without a substrate, as shown schematically in Fig. 1(a). We define the SiNW array to consist

of nanowires of radius a, and height h, arranged in a square lattice with lattice constant d (see Fig. 1). The height of the nanowires is set to the standard thin film photovoltaic thickness of $h = 2.33\ \mu$m. For silicon we use the complex dielectric permittivity of Green and Keevers [28].

Central to our approach is that we express the electromagnetic fields inside the array and outside the array (in free space) in different bases. The fields in free space are expressed in terms of a plane wave basis, whilst within the array the fields are expanded using a Bloch mode basis. In Fig. 1(a) the fields are represent as $\boldsymbol{f}$, if represented in the plane wave basis, and as $\boldsymbol{c}$, if represented in the Bloch mode basis. The advantage of this approach is that the fields are expressed in their natural bases everywhere, greatly reducing the computational cost of the simulations and, critically, providing results in terms of the most intuitive and meaningful basis functions in each domain.

We first solve the electromagnetic wave equation for the Bloch functions of the electric field for an array that extends periodically to infinity in the xy-plane and is infinite and uniform in z. The Bloch functions satisfy the Maxwell equations and the appropriate continuity conditions at the cylinder boundaries and can be written as the product of a function $\phi_{m,\mathbf{k}_\perp,\mathbf{k}_z}(\mathbf{r})$, with the same periodicity as the medium, a phase factor, and a factor representing propagation in the $\pm z$-direction, *i.e.*

$$\mathbf{u}_{m,\mathbf{k}_\perp,\mathbf{k}_z} = \phi_{m,\mathbf{k}_\perp,\mathbf{k}_z}(\mathbf{r})e^{i\mathbf{k}_\perp \cdot \mathbf{r}}e^{i\mathbf{k}_z z}. \tag{1}$$

Here the Bloch modes are indexed by mode number m, $\mathbf{k}_z$ is the z-component of the wavevector, and $\mathbf{r}$ is the in-plane position vector. $\mathbf{k}_\perp$ is the in-plane wavevector that is in the first Brillouin zone, being set by the angle of the incidence. We calculate the Bloch modes using a vectorial FEM routine that discretizes the wave equation to form a generalized eigenvalue problem. The propagation constant $\mathbf{k}_z$ and modal field amplitudes are represented by the eigenvalue and eigenvector respectively and are found using standard algebraic techniques. The FEM routine is based on previous work on optical fibers [29], extended to include periodic boundary conditions.

Having found the modes of the infinite array we proceed to the finite length array by including the top and bottom interfaces. We do this analagously to the procedure for a Fabry-Pérot cavity, which shares the essential feature of a cavity-type structure surrounded by two infinite media. We calculate the scattering matrices at each interface, which represent how energy is reflected or transmitted [30]. The computation of the scattering matrices with fields expressed in different bases requires the projection of each onto their counterpart, with the solution being sought in a least squares sense [30]. Finding the solution requires that we have an orthogonality relationship for the Bloch modes, which is complicated by the algebraic eigenvalue problem being in general non-Hermitian, irrespective of the presence of loss. To establish an orthogonality condition we calculate the adjoint set of Bloch modes—satisfying the same differential equation but with $\mathbf{k}_\perp \rightarrow -\mathbf{k}_\perp$ [31]. Having already found the Bloch modes, the scattering matrices are then calculated from the overlap integrals of the incident plane waves with the Bloch modes.

The scattering matrices are written as $\mathbf{R}_{ij}, \mathbf{T}_{ij}$, where fields are incident from medium i into medium j. The diagonal matrix $\mathbf{P} = \text{diag}[e^{i\mathbf{k}_{z,m}h}]$ represents propagation of each of the modes through a layer of thickness h. We then find the total transmission matrix in terms of the scattering and propagation matrices (where free space and the array are labeled as media 1, 2 respectively) as

$$\mathbf{T} = \mathbf{T}_{21}\mathbf{P}(\mathbf{I} - \mathbf{R}_{21}\mathbf{P}\mathbf{R}_{21}\mathbf{P})^{-1}\mathbf{T}_{12}, \tag{2}$$

with an analogous expression for the total reflection, $\mathbf{R}$. These matrices express the total transmission through and reflection off the array for each plane wave order. The absorptance $A(\lambda)$ is found as the difference between unity and the sums of the square magnitudes of the elements of $\mathbf{T}, \mathbf{R}$ corresponding to propagating waves.
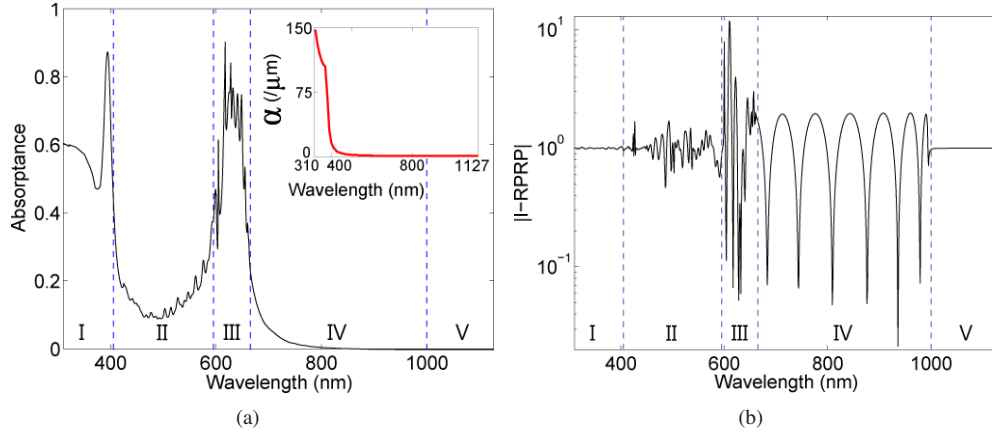
Fig. 2. Simulation results for the dilute SiNW array, over the solar spectrum; 310 nm–1127 nm, calculated at 0.5 nm wavelength intervals. Distinct wavelength regions are labeled with roman numerals. (a) Absorption spectrum, with insert showing the absorption coefficient of bulk silicon (α). (b) Fabry-Pérot resonance calculation where resonances occur at the minima of Eq. (4).

To determine the suitability of various SiNW array designs as solar cells we calculate their *ultimate efficiencies*, η. The ultimate efficiency, as defined by Shockley and Queisser [32], assumes an ideal process where every absorbed photon with energy larger than the electronic band gap produces exactly one electron-hole pair with energy hc/λ_g, where λ_g is the wavelength corresponding to the electronic band gap. The ultimate efficiency then represents the fraction of the incident solar energy, $I(\lambda)$, (taken as the ASTM Air Mass 1.5 direct and circumsolar spectrum [33]) absorbed and converted to electrical energy by the ideal process:

$$\eta = \frac{\int_{\lambda_l}^{\lambda_g} I(\lambda) A(\lambda) \frac{\lambda}{\lambda_g} d\lambda}{\int_{\lambda_l}^{\lambda_u} I(\lambda) d\lambda}. \tag{3}$$

Here $\lambda_l = 310$ nm is where the solar irradiance is negligibly small, $\lambda_u = 4000$ nm is the upper limit of the available data for the solar spectrum and $\lambda_g = 1127$ nm is the band edge of bulk silicon.

3. Analysis of a Dilute Array

To examine the absorption mechanism in detail, we focus on a SiNW array, hereafter referred to as the *dilute* array, consisting of nanowires of 60 nm radius, spaced with a 600 nm period, such that the silicon fill fraction is $\pi a^2/d^2 = 3.1\%$ (with 96.9% air background). The absorption spectrum of this array is shown in Fig. 2(a) for normally incident light, where $\mathbf{k}_\perp = 0$ at the center of the Brillouin zone. For normally incident light the absorption spectrum is polarization independent [34]. We observe a remarkable absorption peak between 595–665 nm, well beyond the strong absorption region of bulk silicon (shown in the insert of Fig. 2(a)) and that the absorption decreases below 595 nm before returning to higher values at 405 nm.

3.1. Absorbing Modes

Using our modal approach we find that the absorption peak, and spectrum in general, are determined by a small subset of the array's modes. These must satisfy three criteria to be highly
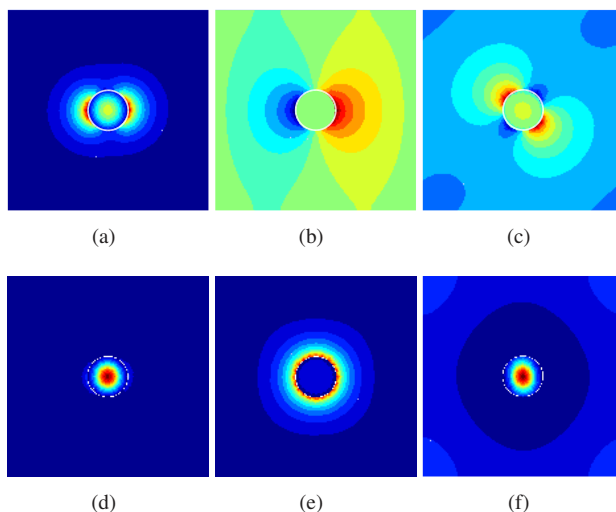
Fig. 3. (a)–(c) Field distributions, of the dominant transverse electric field component, and (d)–(f) energy distributions ($\mathrm{Re}(\varepsilon)||\mathbf{E}||^2$), at the absorption peak wavelength of 617 nm. Field plots are normalized between -1 (blue) and 1 (red), and energy plots are normalized between 0 (blue) and 1 (red). Bloch modes shown are; (a,d) the fundamental mode #1, (b,e) mode #3 and (c,f) the key mode #4.

absorbing; they must (i) be well coupled to by the incident plane waves, (ii) strongly resonate between the top and bottom interfaces, and (iii) concentrate their energy within the silicon nanowires. Note that the modal properties related to (i)–(iii) are wavelength dependent, and that criterion (iii) influences (i).

The set of strongly absorbing modes are referred to as the *key* modes of the array, and we find that these modes often feature slow light regions that complement criteria (i)–(iii) to enhance their absorption further. In addition to the key modes, the fundamental mode, which is roughly equivalent to that of a single nanowire (*i.e.*, an optical fiber), contributes moderately to the absorption at longer wavelengths. The fundamental and key modes evolve distinctly with wavelength and we explain the absorption spectrum fully in terms of how the modes fulfill the absorption criteria (i)–(iii) across the wavelength range. We first examine the criteria (i) through (iii) and then investigate the properties of the key modes as expressed in the dispersion diagram of the array.

3.2. Coupling

The coupling to modes is determined by their symmetry: to couple to an incident plane wave at normal incidence, a Bloch mode must have an even in-plane field distribution, corresponding to the plane waves. Applying this condition to the dilute array reveals that the fundamental mode and one key mode (each of which are two-fold degenerate) are the only absorbing modes, their coupling being at least an order of magnitude stronger than that of all other modes. The existence of only one key mode makes the dilute array ideal for our analysis. Figures 3(a)–3(c) show the field distributions of the dominant transverse electric field component at the absorption peak wavelength of 617 nm, for the fundamental mode #1, mode #3 and the key mode #4, where enumeration is by the modes order of cut-off (see Fig. 5(b)). The field plots illustrate the even/odd symmetry of the modes, which allows the fundamental and key modes to be coupled to the incident field, but forbid the coupling to mode #3 at normal incidence.
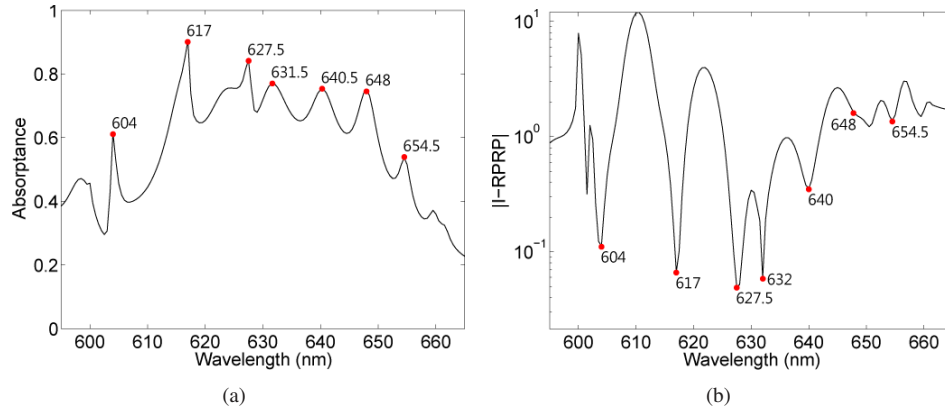
Fig. 4. (a) Absorption spectrum and (b) Fabry-Pérot resonances, in region III, for the dilute array. The wavelengths of features are marked and show excellent agreement for almost all points.

3.3. Resonances

The second criterion for high absorption by light trapping is that a mode undergoes strong Fabry-Pérot resonances. These are the natural resonances of the array, which shares the essential form of a dielectric thin film bounded by infinite media. The calculation of these resonances is instructive since they relate directly to the undriven system, rather than to the driven system, where insights are sought from the complex absorption response of the array under illumination. The Fabry-Pérot resonance condition is that a Bloch mode is unchanged after circulation, having been reflected off the top and bottom interfaces. In our formulation this condition is expressed as the minimization of

$$\det\left(\mathbf{I} - \mathbf{R}_{21}\mathbf{P}\mathbf{R}_{21}\mathbf{P}\right). \tag{4}$$

Figure 2(b) shows the values of the Fabry-Pérot resonance condition across the wavelength range, where distinct regions are labeled with roman numerals I–V, which are also shown in Fig. 2(a).

In the long wavelength limit (region V) the only propagating mode is the fundamental mode, which is poorly confined within the nanowires leading to low reflection at the end of the array, leading to very weak Fabry-Pérot resonances. In region IV sharp resonances occur, however these do not lead to absorption features because the only resonant mode in region IV is mode #3 which couples poorly to the SiNW array modes. The transition to region III is marked by a steep increase in absorption and a distinct change in the resonance behavior. The cause of this change is the presence of the key mode, the cut-off of which is at 665 nm. This mode fulfills the requirements (i)–(iii) for strong absorption, and its Fabry-Pérot resonances are directly observable in the absorption spectrum peaks, as shown in Fig. 4. The higher background values in Fig. 4(b) around 650 nm are caused by the off-resonance behavior of mode #3, as seen in Fig. 2(b).

In addition to these single Bloch mode resonances there exist composite resonances, where energy is coupled from one absorbing mode into another through the reflection matrix $\mathbf{R}_{21}$. These occur as a valid solution of the continuity requirements at the top and bottom interfaces. Such resonances further enhance light trapping and absorption in region III, where they involve the fundamental and key modes.

At shorter wavelengths we see reduced resonances and absorption in region II and strong absorption in the absence of resonances in region I. The latter is due to the increase in bulk

silicon's absorptance (see Fig. 2(a) insert), which dampens resonances but ensures that all light entering the array is absorbed in a single pass. To understand region II we now examine the energy concentration of the modes.

3.4. Energy Concentration

Since light can only be absorbed by the silicon, the fraction of a mode's energy concentrated within the nanowires is intrinsic to its ability to contribute to the array's absorption. We define an energy concentration fraction $\mathscr{C}$ as,

$$\mathscr{C} \equiv \frac{\int_{\text{nanowire}} \text{Re}(\varepsilon) ||\mathbf{E}||^2 \text{dA}}{\int_{\text{unitcell}} \text{Re}(\varepsilon) ||\mathbf{E}||^2 \text{dA}}, \tag{5}$$

where dispersive effects are neglected. Figure 5(a) shows $\mathscr{C}$ for the fundamental mode (blue) and for the key mode (red), overlaid on the absorption spectrum.

The fundamental mode is seen to evolve like the fundamental mode of an optical fiber: it propagates for all wavelengths and is drawn into the higher refractive nanowire with decreasing wavelength. As its energy concentration increases around 850 nm, we see a gradual increase in the absorption. In region III the moderate concentration (see Fig. 3(d)) allows for good coupling to the plane waves and the mode contributes to the absorption peak by resonating both independently and together with the key mode. When, at shorter wavelengths, the concentration within the very thin nanowires exceeds approximately 90% the coupling of the unfocused normally incident light to the tightly confined mode is reduced [35], such that the fundamental mode contributes little to the absorption in regions I and II. Mode #3 is poorly confined to the nanowires (Fig. 3(e)) and is not coupled to because of its symmetry mismatch to the plane waves (Sect. 3.2)

The key mode evolves in a different and unexpected way: it has a substantial energy concentration after cut-off, but this decreases in region II before rapidly increasing in region I. The key mode dominates the absorption, so that the absorption spectrum essentially follows its energy concentration fraction: moderately large energy concentration (see Fig. 3(f)) coincides with strong resonances and absorption (region III); when its energy fraction takes small values while the coupling remains high (region II), energy is merely transmitted through the array. As the energy concentration rises around 410 nm the absorption increases sharply until the coupling to the key mode is reduced by its concentration exceeding 90% around 393 nm. In region I there are many propagating modes because of the short wavelengths and the increase in the real part of silicon's refractive index, whilst the steep increase in the imaginary part of the refractive index means that all modes coupled to by the incident field contribute to the absorption.

3.5. Dispersion Diagram

Having analyzed how the coupling, resonance and energy concentration criteria relate to the fundamental and key modes, and how these modes evolve with wavelength, we now investigate further the properties of the key mode through the modal dispersion diagram of the SiNW array. Figure 5(b) shows $\text{Re}(k_z d)$, the real part of the normalized propagation constant, plotted in blue for all but the key mode (red) versus wavelength. The black curve shown in Fig. 5(b) is the light line, where $n_{\text{eff}} = 1$.

The dispersion diagram shows that the key modes have enhanced absorption, over that required by criteria (i)–(iii), due to slow light regions, where light-matter interactions (including absorption) are increased due to higher intensities [36]. Given the choice of axes in Fig. 5(b), we find that the group velocity, v_g, is inversely proportional to the gradient:

$$\frac{dk_z}{d\lambda} = -\frac{\omega^2}{2\pi c} \frac{dk_z}{d\omega} = -\frac{\omega^2}{2\pi c} \frac{1}{v_g}. \tag{6}$$
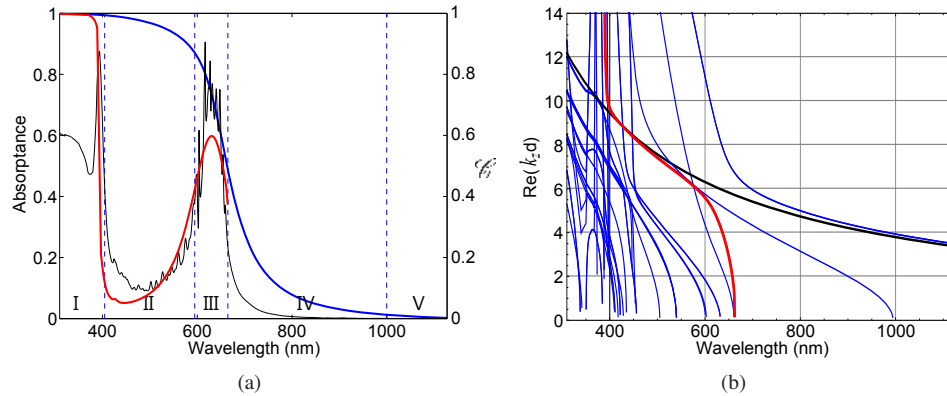
Fig. 5. (a) Energy concentration fraction within nanowires for fundamental mode (blue) and key mode (red), overlaid on absorption spectrum. (b) Modal dispersion curves of $\mathrm{Re}(k_z\,d)$, where $d = 600$ nm, as a function of wavelength. General modes are shown in blue, the key mode is red, and the black line is the light line.

Thus a large gradient of a mode's dispersion curve represents a region of slow energy transport through the array, whilst a small gradient indicates a group velocity close to c, the speed of light in vacuum. The latter occurs when the dispersion curves approach the light line, where most of the mode's energy is in the air ($n_{\mathrm{eff}} = 1$), resulting in weak absorption. For the key mode the group velocity corresponds directly to the energy concentration fraction and inversely to the absorption spectrum; when the group velocity is low (as in regions I, III) the absorption is high (strengthened by Fabry-Pérot resonances) whilst in region II the velocity is high but the absorption is low. The group velocity of the key mode also determines the resonance spacings, with the free spectral range given as $\Delta f = v_g/2h$. Thus the resonances in slow light regions lie close together, overlapping to form the major absorption peak of region III.

Lastly we note that for a single nanowire (optical fiber), bound modes only exist above the light line because they are required to decay away from the fiber. For the SiNW array only the fundamental mode remains in this domain and all other modes undergo cut-off when $\mathrm{Re}(k_z d) = 0$, well below the light line. Their existence here is made possible by the presence of the array, which removes the restriction on modes to decay to zero at infinity. Importantly we see that the absorption peak above 595 nm occurs when the key mode is below the light line.

3.6. Ultimate Efficiency

For photovoltaic applications, the absorption enhancement of SiNW arrays should maximize the ultimate efficiency, as defined in Eq. (3). We find that the broad absorption peak aligns well with the peak of the solar spectrum so that the efficiency of the dilute array is 6.4%. This is less than that of an equally thick thin film ($\eta = 13.8\%$) [12], however when the efficiency is scaled by the volume of silicon used, the dilute array is a remarkable 23 times more efficient than the thin film, as it consist of only 3.1% silicon. To increase the efficiency of SiNW arrays beyond that of the dilute array and a thin film, we require arrays with higher filling fraction. In the next section we consider how the theory for the dilute arrays carries over to such arrays.

4. Analysis of a Dense Array

As our example of a more dense array we take an array with $a = 125$ nm, $d = 495$ nm (20% fill fraction), which has an ultimate efficiency of 15.8%, exceeding that of the thin film. The absorption spectrum of this array, shown in Fig. 6(a), features many sharp, irregularly spaced
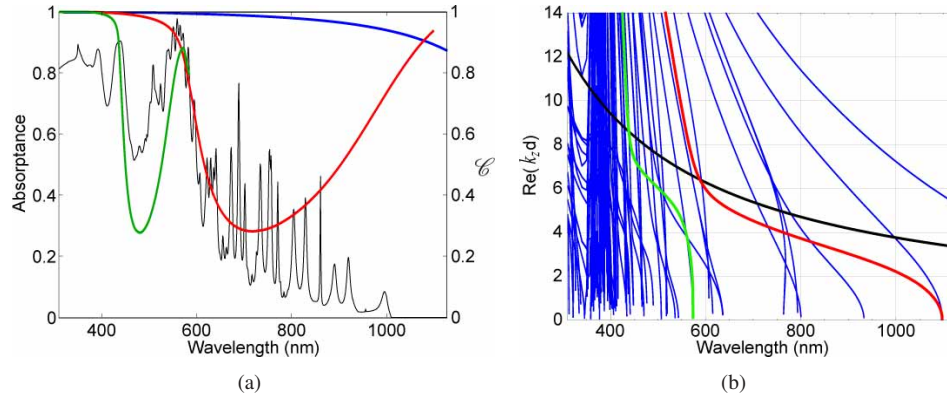
Fig. 6. Results for the dense array with wires of 125 nm radius. (a) Absorption spectrum and energy concentration fraction for the fundamental mode (blue) and key modes B_1, B_2 (red, green). (b) Modal dispersion curves for general modes (blue) and B_1, B_2 (red, green) with the light line in black.

peaks and a broad peak between 500–600 nm. Although the spectrum is significantly more complex than that of the dilute array, it can be understood using the same concepts.

4.1. Effects of Radius and Period

The major effect of increasing the nanowire radius is that the modes shift to longer wavelengths. This is true in general for larger structures, as is well known for optical fibers, where the shift depends on the radius of the core as a/λ. Similarly, we find that increasing the spacing between nanowires of constant radius (thereby decreasing the fill fraction) also shifts the dispersion relation to longer wavelengths.

Comparing Figs. 5(b), 6(b) for the dilute and dense arrays respectively, we see that the effect of increasing the radius exceeds that of decreasing the period, consistent with Fig. 7. Since we deal with a fixed wavelength range, the shift introduces new propagating modes, so that there exist 2 key modes in the dense array, referred to as B_1, and a higher order mode, B_2. In Fig. 6(b) these are seen to cut-off at 1099 nm (B_1, red) and 585 nm (B_2, green). As the number of key modes increases with radius and fill fraction, modal analysis becomes increasingly complicated, however the same physical mechanisms still drive the absorption of SiNW arrays.

The trends of dispersion diagrams are brought out in Fig. 7, which shows the cut-off wavelengths of B_1 versus lattice constant, for various radii nanowires. Shown are results from our FEM calculation of the Bloch modes (as in Sect. 2) as well as an analytic calculation of just the key modes, which shows excellent agreement and will be discussed in Sect. 4.3.

4.2. Dense Array Absorption Spectrum

In explaining the absorption spectrum of the dense array we start at long wavelengths, where key mode B_2 is beyond cut-off, so that B_1 alone determines the absorption (see Fig. 6(b)). At wavelengths below the absorption edge at 1010 nm (above which $\text{Im}(n) = 0$) the Fabry-Pérot resonances of B_1 produce absorption spikes, which are sharp because the mode is only slightly lossy and they are irregularly spaced due to geometric and material dispersion. The low loss of key mode B_1 is a product of its moderate energy concentration in silicon and the small values of $\text{Im}(n)$, whilst the increased spacing between resonances is due to the larger group velocity of B_1, see Sect. 3.5.

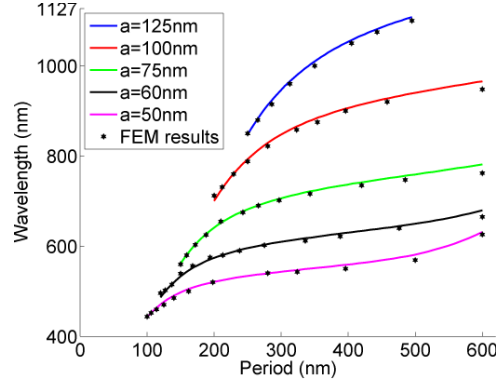As the energy concentration of B_1 increases around 600 nm the mode becomes increasingly

Fig. 7. Cut-off wavelengths of key mode B_1 as a function of lattice constant for arrays of differing nanowire radius. Shown are results from both FEM computations and using a dipole approximation (see Sect. 4.3).

lossy, which broadens its resonances. Although the modes of the dense array reach higher energy concentration fractions than in the dilute array, this does not suppress coupling until the fraction exceeds 0.95, as the fields are confined within a larger nanowire. This suppresses the coupling of the incident fields to the fundamental mode throughout the wavelength range (see the blue curve in Fig. 6(a)).

At 585 nm key mode B_2 cuts off with a high energy concentration and low group velocity, and so together with B_1 creates the broad absorption peak via lossy Fabry-Pérot resonances. The short wavelength side of the absorption peak is marked by the energy concentration of B_2 going through a trough, in so doing contributing significantly to the transmission through the array, at the cost of the absorption. This reduction is not as large as in the dilute case because there is still a well absorbing key mode, and the minimum concentration fraction of B_2 is higher. As for the dilute array the real and imaginary components of silicon's refractive index increase around 400 nm and light is efficiently absorbed.

4.3. Dipole Model for Key Mode Cutoff

Because the appearance of the key modes determines the long-wavelength edge of the main absorption peak, it is useful to estimate the cut-off wavelength of these modes. Examination of the fields of the key modes reveals that the z-components of both electric and magnetic fields are predominantly dipolar. This suggests that the fields can be written to a good approximation as

$$E_z(r,\theta) = \begin{cases} C^E J_1(k_1 r)e^{i\theta} & \text{for } r < a \\ \left[A^E J_1(k_2 r) + B^E H_1(k_2 r)\right]e^{i\theta} & \text{for } r \geq a \end{cases} \tag{7}$$

where $k_1 = (\varepsilon_1 \omega^2/c^2 - \mathrm{k}_z^2)^{1/2}$, $k_2 = (\varepsilon_2 \omega^2/c^2 - \mathrm{k}_z^2)^{1/2}$, the quantities ε_1 and ε_2 are the permittivities of the nanowire and background respectively, and J_1, H_1 are the Bessel and Hankel functions of the first kind [37]. The magnetic fields may be expressed in a similar form. Such an approximation would be expected to hold for nanowire arrays that are sufficiently dilute ($a/d \ll 1$) that higher-order multipoles are not necessary for a true representation of the field contributions from the other cylinders in the array. The coefficients A, B and C can be eliminated from the expansion by enforcing the appropriate field continuity conditions at the cylinder boundaries. The effect of the lattice can be taken into account using the Rayleigh identity (including only dipole terms) to find

$$A_1^{E,H} = S_0(k_2,\mathbf{0})B_1^{E,H}, \tag{8}$$

where S_0 is the zero-th order lattice sum [37], defined as a sum over the set of all lattice vectors $\mathbf{R}_p$ in the array

$$S_0(k_2, \mathbf{k}_\perp) = \sum_{p \neq 0} H_0(k_2|\mathbf{R}_p|)e^{i\mathbf{k}_\perp \cdot \mathbf{R}_p}. \tag{9}$$

Fast techniques for summing this slowly-converging series are given in [38]. Solving the resulting linear system leads to a transcendental equation for the cut-off wavelength, *i.e.* the wavelength at which $\mathrm{k}_z = 0$ for the key modes,

$$\frac{\varepsilon_1}{k_1}\frac{J_1'(k_1 a)}{J_1(k_1 a)} - \frac{\varepsilon_2}{k_2}\frac{H_1'(k_2 a) + S_0 J_1'(k_2 a)}{H_1(k_2 a) + S_0 J_1(k_2 a)} = 0, \tag{10}$$

where primes denote derivatives with respect to the argument. The simple dependence on the lattice sum S_0 allows for easy variation of the lattice type by exchanging S_0. For a single isolated wire $S_0 = 0$; in this case there are no real solutions to Eq. (10). This reiterates the finding of Sect. 3.5 that the existence of the key modes is supported by the lattice geometry.

As seen in Fig. 7, there is excellent agreement between the approximation given by the solution of Eq. (10) and the full numerical simulation, even for relatively high filling fractions. Interestingly the approximate model also predicts the cutoffs of the second order key modes. This analytic calculation is therefore a promising design tool for estimating the position of absorption peaks in nanowire arrays.

5. Off-Normal Incidence

The results and discussions of the last two sections have been limited to normal incidence, for which all polarization states and azimuthal angles are degenerate. For photovoltaic applications the absorption behaviour with angle of incidence is important, especially for inexpensive, moderate efficiency designs, which are to be mounted on a fixed platform. For such PV modules the sun daily traces an arc through polar angles and a range of azimuthal angles depending on the season and latitude. For the unpolarised sunlight incident on the array we consider both s and p polarizations and unlike previous studies [12, 20–22] also the effect of the orientation of the lattice to these polarizations. The latter is taken into account by calculation of light parallel to, and at 45° to the lattice vector, labeled (10) and (11) respectively, as shown in the insert of Fig. 9. We first discuss the effect of angle of incidence on the modes of the array, and then calculate the variance in ultimate efficiency across polar angles.

Figures 8(a) and 8(b) show the absorption spectra of the dilute array at 20° off-normal, where the general features of normal incidence (shown as a broken line) remain and additional peaks occur at long wavelengths. The two polarizations are absorbed differently because they couple to the different key modes (the degeneracy of which is broken at off-normal incidence). For both polarizations the long wavelength edge of the major absorption peak remains at 665 nm, as both key modes undergo a rapid increase in their energy concentration below this wavelength, after cutting off at 825 and 740 nm. At off-normal incidence the even symmetry of the plane waves is broken, allowing more Bloch modes to be coupled into. This is demonstrated by the long wavelength absorption peaks which are the Fabry-Pérot resonances of mode #3. The symmetry of these modes is such that they are only coupled into at non-normal incidence. Consistent with the argument of Sect. 4 we attribute the sharpness of the peaks to low loss and the large spacing between peaks to a high group velocity.

The absorption spectrum of the dense array (Figs. 8(c) and 8(d)) undergoes a significant change, as the cut-off of B_2 shifts to around 805 nm, where it has a high energy concentration, thus producing an additional broad peak. The characteristic evolution of key modes follows, with an absorption low between 600–700 nm, before another broad peak below this, once B_2 passes through the light line.
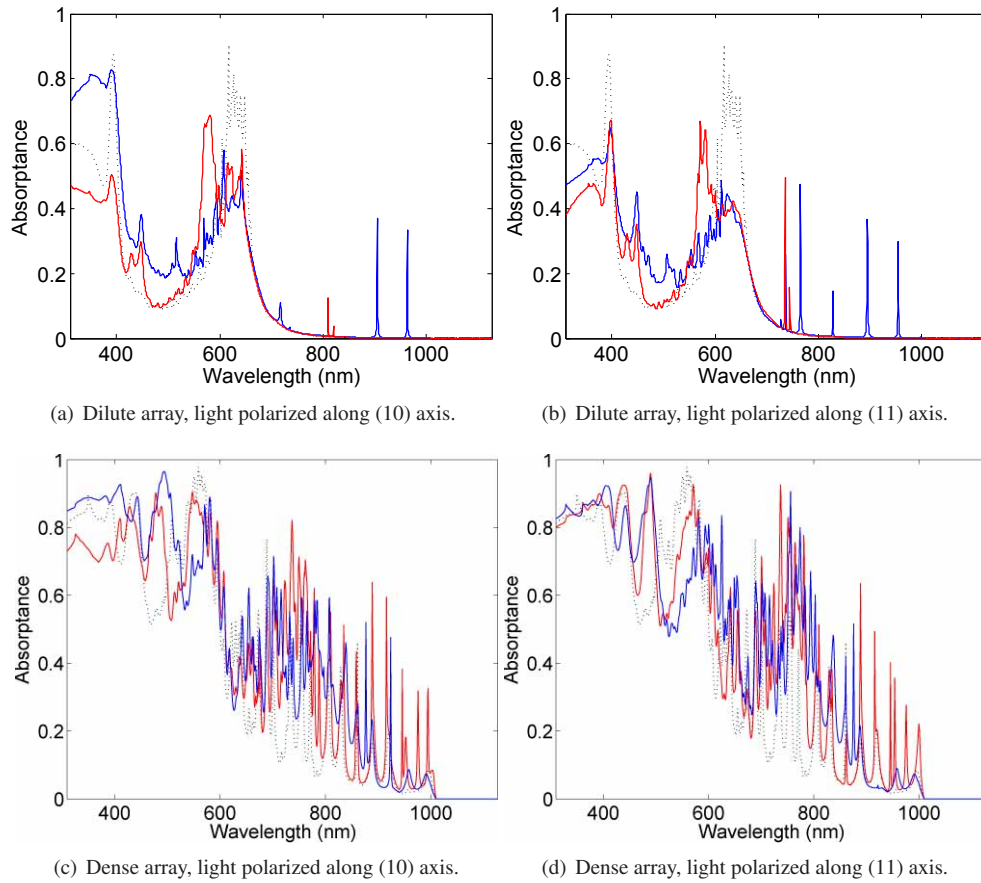
(a) Dilute array, light polarized along (10) axis.

(b) Dilute array, light polarized along (11) axis.

(c) Dense array, light polarized along (10) axis.

(d) Dense array, light polarized along (11) axis.

Fig. 8. Absorption spectra at $20°$ off-normal. The red and blue lines are s and p polarized incident fields respectively and the dashed black curve is for normal incidence.
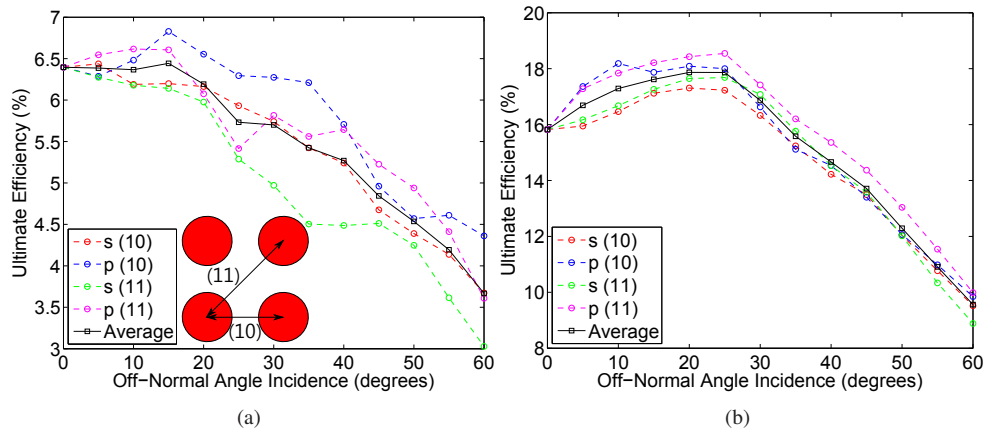

(a)

(b)

Fig. 9. Ultimate efficiency with off-normal angle of incidence for (a) the dilute and (b) the dense arrays. The insert shows the vectors (10) and (11).

To quantify the angular performance of SiNW arrays, we calculate the ultimate efficiency of the dilute and dense arrays for polar angles 0–60°. Figure 9 shows the efficiency with off-normal angle θ, where the reduced projection of the sunlight to the arrays surface is incorporated by a scaling of $\cos(\theta)$, and the average of the polarizations and orientations is shown in black. We find the average efficiency to remain high across the angular range, dropping by less than $\cos(\theta)$ for both arrays. For the dense array the additional broad peak increases the efficiency above the normal incidence value for angles up to 30° off-normal. Consistent with previous studies [12] we find the efficiency of p polarized light to be in general higher than s polarized light, due to higher absorption at short wavelengths.

6. Conclusion

We have presented a comprehensive description of the optical absorption mechanism of SiNW arrays. We used a novel, semi-analytic modal method, which allows for the identification of a small set of key modes that dominate the absorption. The excellent absorption of these modes is due to their good coupling to the incident plane waves, high energy concentrations within the nanowires, and strong Fabry-Pérot resonances between the top and bottom interfaces. By studying the evolution of the key modes with wavelength (particularly their energy concentration), we explain the various features of the absorption spectra of a dilute and dense array, including the sharp and broad resonances peaks. These characteristics are elegantly predicted by the group velocity of the modes, where we showed slow light regions to result in decreased resonance spacing and enhanced absorption due to higher intensities.

Our detailed knowledge of the key modes allowed us to develop an analytic approximation to accurately predict their cut-off wavelength as a function of nanowire radius and lattice constant. This approximation may be used to efficiently design SiNW arrays and it highlights that the key modes are inherently a feature of the periodic array. We showed that the behaviour at off-normal incidence was also determined by the key modes and that the ultimate efficiency of the arrays remained high (or increased) at irradiance at up to 60° off-normal.

Having determined the absorption process of SiNW arrays to be related to a few Bloch modes we may now manipulate these by modifying the geometry, so as to optimize the absorption. Geometries which we can model include arrays of different lattice type, the inverse structure of air holes in a silicon background [39], touching cylinders [40], and arrays composed of nanowires of various radius or arranged quasi-randomly by using a supercell [19]. Modification of the scattering matrices will also allow for the simulation of a SiNW array on a substrate.